

The Impact of Dopant Compensation on Graded p-n Junctions in Si Nanowires

Iddo Amit^{1,†}, Nari Jeon^{2,†}, Lincoln J. Lauhon² and Yossi Rosenwaks^{1,*}

¹Department of Physical Electronics – School of Electrical Engineering, Tel Aviv University, Ramat Aviv 69978, Tel Aviv, Israel.

²Department of Materials Science and Engineering, Northwestern University, Evanston, Illinois 60208, United States.

[†]These authors contributed equally to this work.

Corresponding author: yossir@eng.tau.ac.il

KEYWORDS: Nanowire, Diode, Doping, Kelvin probe force microscopy, Vapor-Liquid-Solid Growth, Dopant compensation

Abstract

The modulation between different doping species required to produce a diode in VLS-grown nanowires (NWs) yields a complex doping profile, both axially and radially, and a gradual junction at the interface. We present a detailed analysis of the dopant distribution around the junction. By combining surface potential measurements, performed by KPFM, with finite element simulations, we show that the highly doped ($5 \times 10^{19} \text{ cm}^{-3}$) shell surrounding the NW can screen the junction's built in voltage at shell thickness as low as 3 nm. By comparing NWs with high and low doping contrast at the junction, we show that dopant compensation dramatically decreases the electrostatic width of the junction and results in relatively low leakage currents.

1. INTRODUCTION

Nanowire p - n junction diodes are expected to play a major role in future nanoelectronics, as diodes form one of the fundamental active components in solid state devices. Nanowire (NW) p - n junctions have been realized using various fabrication methods, including ion implantation on pre-grown nanowires,¹ contact doping of intrinsic wires by two precursor bearing wafers,² and *in-situ* doping, which can produce either axial or radial junctions.^{3,5} Over the last few years, nanowire growth techniques have improved significantly, mainly due to a better understanding of the chemical processes occurring at the liquid catalyst^{6,8} and the surface chemistry governing the incorporation of dopant species through side-wall deposition.^{9,10} However, while the synthesis methods continue to improve rapidly, correlation between the chemical composition and the electronic characteristics is less common and remains challenging due to sensitivity of properties to minute concentrations of dopants and impurities, and the possibility of dopant deactivation and compensation.^{11,12} While analytical methods exist to measure both active and inactive dopants, device output characteristics do not directly reveal the active doping fraction.

The performance of some recently reported homojunction devices has been correlated with the underlying dopant distribution. For example, Vallett *et al.* demonstrated, using scanning capacitance microscopy (SCM), the analysis of a nanowire-based tunnel field-effect transistor (TFET) that exhibits an abrupt junction.¹³ While the SCM method can be extremely sensitive to the location of the electric junction, it can significantly underestimate the width of depletion regions.¹⁴ Nevertheless, obtaining a high-quality functional diode, *i.e.* a diode with low leakage (reverse) currents and low resistance, requires a well-defined and abrupt junction to form between its segments.¹⁵⁻²⁰ Therefore, a quantitative analysis of the active doping levels in the different segments of the device, decoupled from the chemical composition, is still required to understand electrostatic junction formation at nanostructured devices.²¹

One of the major challenges encountered with *in-situ* dopant modulated growths is the formation of diffused boundaries between different segments. This phenomenon is a direct result of the “catalyst reservoir effect”,^{6,7,10} where dopant atoms remain dissolved in the

liquid catalyst for relatively long time after their gaseous source flow into the reaction chamber has been terminated. The dissolved atoms are then continuously incorporated into the solid, forming a slow decay profile along the growth axis, thus forming a gradual junction that results in high reverse bias saturation currents and low on/off ratios. Recently, groups have made improvements in junction abruptness through adjustments in growth conditions by reducing the solubility of dopant species in the catalyst^{8,22} or even slowing down the growth rate to allow dopant evaporation from the catalyst during growth.⁷ However, it is in general difficult to achieve growth conditions that are optimal for both dopant species in a homojunction. Furthermore, surface doping from the background gases in the reactor is a common outcome, leading to the formation of a surface region that is enriched in dopant. Such surface doping can be suppressed by the introduction of reactive, corrosive species such as HCl²³ at the cost of increasing the complexity of recipes and the need for maintenance. Even with the advances noted above in improving junction abruptness and radial doping uniformity, doping profiles are never perfectly abrupt nor perfectly uniform, so it remains necessary to understand the impact of nanoscale doping profiles on nanowire device properties.

Here we present a detailed analysis of *in-situ* doped, SiNW-based *p-n* diodes, where the doping source was modulated during growth to produce both *p-i-n* and *p-n* junctions. Surprisingly, despite the influence of both the reservoir effect and surface doping from the vapor phase, Kelvin probe force microscopy (KPFM) measurements of the surface potential reveal that the electrostatic junction width is less than the KPFM resolution (~ 30 nm). The electrostatic consequences of complex doping profiles are revealed by using the intrinsic segment in the *p-i-n* NW as a buffer zone to partially deplete the catalyst reservoir of one dopant species before the introduction of the next species into the system. Hence, the doping of the two segments should in principle be decoupled. Despite the presence of a highly doped shell that screens the electrostatic characteristics of the underlying junction, the NWs exhibit a typical diode behavior, with small leakage currents. The combined *I-V* and KPFM measurements prove that despite the strong influence of the catalyst reservoir effect, the resulting junction is, electrostatically, more abrupt than expected due to compensation effects. The catalyst reservoir effect on the electronic performance of a

junction becomes significant in the *p-i-n* structure, where the nominally intrinsic segment is found to be rather highly doped with boron. By solving the Poisson equation for the device, we establish the VS shell thickness and doping density, as well as the doping densities in the NW core and their radial profile. We show that an informed design of the doping modulation in a NW junction can produce a high-quality diode, despite the seemingly unintended contribution from the VS mechanism and the catalyst reservoir.

2. EXPERIMENTAL SECTION

The fabrication process used to produce the nanowires for the experiments reported here followed the same technique and procedure which was previously described.^{10,24-26} In brief, the SiNWs were grown in a hot-wall low-pressure chemical vapor deposition (LPCVD) using 80 nm Au nanoparticles (AuNPs) as catalysts, high-purity silane (SiH₄) as the precursor gas for the silicon, and phosphine (PH₃, 200 ppm diluted in He) and diborane (B₂H₆, 100 pp, diluted in He) as the P and B dopant precursors, respectively. Hydrogen (H₂) was used as the carrier gas with 20 SCCM for p-type and intrinsic segments, and with 200 SCCM for n-type segment. Silane flow rate was 4 SCCM for p-type and intrinsic segments, and 2 SCCM for n-type segment. For *n*- and *p*-type segments, Si:P ratio of 1000:1 (phosphine flow rate of 10 SCCM) and Si:B of 3000:1 (diborane flow rate of 6.67 SCCM) were used, respectively. The p-type and intrinsic segments were grown at 460 °C and the n-type segment were at 420 °C.^{7,27} The temperature started to decrease with the initiation of phosphine flow, and it decreased and stabilized at 420 °C within ~3 minutes. The pressure was kept at 40 Torr for the entire growth. The growth conditions were chosen to enable a taper-free growth for a relatively long period.

Fig. 1 (a) and (b) schematically shows the *p-i-n* and *p-n* NWs' configuration and growth order, respectively. For clarity, the figures are shown in a stepwise illustration from left to right. Of the two doping species, it is well known that diborane produces thicker vapor-solid (VS) grown shells around the NW, and is more challenging to control.²⁸ In order to reduce the screening effect of a thick, highly doped shell over the entire NW, the B doped (*p*-type) region was grown first as shown in the left panel of Figs. 1 (a) and (b), near the NWs base, surrounded by a B doped shell. Next, an intrinsic region was grown on top of

the B doped segment (middle panel of Fig. 1 (a)), by shutting down the B_2H_6 flow into the reaction chamber. This step was omitted in the p - n NW. It is, however, important to note in light of the results reported in Ref. [10], that while the intrinsic part was growing, B atoms were still dissolved, in high concentration, in the liquid catalyst, thanks to the reservoir effect, and were still being incorporated into the grown segment. Indeed, our results will show that the intrinsic region presents a medium- to highly-doped behavior. Finally, a P doped (n -type) segment was grown at the top of the wire (right panels of Figs. 1 (a) and (b)). It is reasonable to assume that while the n -type part is growing, both P and B atoms are dissolved simultaneously in the catalyst. However, while the P atoms are supplied to the catalyst from a constant source by maintaining a constant vapor pressure in the reaction chamber, the B atoms are slowly depleting from the catalyst. Therefore, the last segment is initially a compensated n -type doped NW. As the final n -type segment is growing, a thin but highly P-doped shell forms on top of the two previously grown segments, resulting in the complex core-multishell structure described in the right panel of Figs. 1 (a) and (b). The resulting NWs were about 20 μm long, equally partitioned between their comprising segments.

To incorporate the NWs into single NW devices, a NW dispersion in isopropanol was prepared using an ultrasonic bath and then dropcast onto a wafer pre-patterned with electrodes and alignment marks. Next, each individual NW was connected to a unique set of electrodes by electron beam lithography, and 120 nm of Ni was deposited as the electrode metal. Prior to the metal deposition, the wafers were treated with an oxygen-plasma asher to remove the electron resist residues and with buffered oxide etch to remove the native oxide to allow good electric contact. The single nanowire devices were used for both transfer and KPFM measurements. The wafer on which the NWs were deposited formed the backgate terminal and was grounded throughout the measurements. The KPFM measurements were conducted using a Dimension Edge AFM system (*Bruker AXS*) and a Pt-Ir-coated highly doped silicon tip (PPP-EFM, *Nanosensors*) operating in the “dual frequency mode”, where the topography is scanned at the first mechanical resonance frequency (f_0) of the cantilever, and the contact potential difference is measured simultaneously by electrically exciting the tip at the first overtone of its resonance

frequency ($\approx 6.2 \cdot f_0$).

3. RESULTS AND DISCUSSION

Fig 2 (a) shows the transfer characteristics of a single *p-i-n* NW device. The reverse current is actually smaller than what is shown in Fig 2 (a) due to the amplifier settings used. The reverse (saturation) current is constant, with indication of a small positive current offset in the amplifier. The constant leakage current shows that there are no shunt or leakage currents across the nanowire. We note that the measured current-voltage characteristics result from doping gradients in three dimensions and cannot therefore be satisfactorily described using the simplified Shockley equation. For example, one cannot rely on the slope-over point to determine the built-in potential, as the contact resistance and the screening effect of the shell render the conventional models inadequate. Nevertheless, the presence of a built-in potential difference, which is evident from the rectifying behavior of the devices, allows us to discuss the device using the conventional diode terminology. In forward bias, the device behavior qualitatively resembles that of a diode connected in series with a constant resistor, but a closer examination of the curve shows that the current slope is changing continuously over the voltage range for which the diode dominates, indicating that the bias drops over at least two junctions in the device. The two regimes of different resistance are marked by the dashed red lines in Fig. 2 (a): the first represents the bias range over which one of the diodes still contributes significantly to the total resistance, and the second represents the regime in which the device series resistance ($\sim 2 \text{ M}\Omega$) is the dominant resistance. These observations are corroborated by the results of the KPFM measurements described below.

The transfer characteristics of the *p-n* junction NW are shown in Fig. 2 (b). The constant slope in forward bias (positive bias values) show that the NW consists of a single junction, with a higher resistance ($\sim 4 \text{ M}\Omega$) than the resistance measured for the *p-i-n* diodes. Numerical simulations show that band-to-band tunneling currents in this nanowire are negligible, as described in the Supporting Information and discussed further below. By establishing the diode polarity through the *I-V* measurements, we were able measure the surface potential of the diode under reverse bias with KPFM. The KPFM uses a highly

conductive AFM tip as a Kelvin probe to measure the contact potential difference (CPD), which is defined as $CPD \equiv -(\Phi_t - \Phi_s)/q$, where Φ_t and Φ_s are the tip and sample work functions, respectively, and q is the elementary charge.²⁹ Fig. 3 shows the topography (a), CPD of a grounded device (b), and CPD under reverse bias (c) for a single *p-i-n* device. For both KPFM images, only the relevant part of the wire around the junction is shown. The NW topography (Fig 3 (a)) changes along its axis. On one end of the junction (right hand side of the image), the NW appears to be slightly rougher than on the other side. The rough side, which will later be identified as the boron doped region, was observed in all the measured wires. These results are in agreement with previous studies that attributed polycrystalline shell growth to the presence of B_2H_6 .²⁸ However, these defects seem to bear little to no importance for the NW potential profiles.

The CPD image of the grounded device (Fig. 3 (b)) shows relatively constant surface potential across the NW, which is an indication of constant surface doping. The surface is in fact uniformly doped as a result of the unintentional VS growth mechanism, which forms a thin, highly P-doped shell over the entire NW during the third growth step. It is important to note here that the constant surface potential over the wire means that the P-doped shell screens the underlying doping modulation completely, an effect which can be attributed to the VS shell's thickness and/or its high doping level.

Under reverse bias, the device shows an abrupt change in surface potential along the wire where the junction forms (Fig. 3 (c)). Apparently, the application of a reverse bias depletes the VS shell so that it no longer screens the underlying junction, and we observe that the higher work function is associated with the *p*-type (right hand) side, whereas the low work function on the opposite side is associated with the *n*-type side. At reverse bias, the VS shell becomes depleted quickly, reaching an electron density of 10^{10}cm^{-3} that prevents it from acting as a shunt pathway, accounting for the low leakage currents shown in Fig. 2. Surprisingly, there is no gradual change in surface potential that we expect to see in the intrinsic region, which should be depleted of mobile carriers. Instead, there is an abrupt change in potential at the onset of the *n*-type region. We propose that the nominally intrinsic segment is, in fact, a lightly doped *p*-type segment due in part to doping from the catalyst reservoir, and that the majority of the potential applied to the system drops across an

electrostatically abrupt p - n junction at the terminus of the nominally intrinsic region, as is also evident from the position of the junction.

Fig. 3 (d) shows the CPD profiles of a p - i - n NW measured along the NW axis between both electrodes, at different reverse biases. Here we can directly observe the two junctions that were implied from the I - V curve. The first junction, which is marked by a red dashed rectangle, is the p - n junction, and the second junction (marked by a blue dashed rectangle) is a Schottky junction formed at the metal–nanowire interface. There are three major points evident from Fig. 3 (d). First, it is clear that there is, indeed, a constant surface potential (black curve) at zero bias, which implies that the VS shell is of sufficient thickness and phosphorus concentration to completely screen the underlying built-in potential. Second, the depletion region width, indicated by the band bending around the p - n junction, is less than a micron wide. Third, a Schottky junction forms at the p -type terminus of the wire, as a result of the rather complex core–multishell–metal (p - p^+ - n -metal) structure.

The CPD profiles of the p - n NW, measured between the two electrodes, are shown in Fig. 3 (e). In general, the CPD profiles are very similar to the profiles of the p - i - n NWs. However, there are a few minor differences between the two devices. The measurements in Fig. 3 (e) show a significantly lower Schottky barrier at the metal- p -type region. This is also indicated by the potential drop over the p region that is a direct result of the lower contact resistance. More importantly, the CPD measurement shows that when both electrodes are kept grounded (black curve), there is a pronounced built-in voltage of 0.2 V between the two parts of the wire. We note that for a junction formed between two highly doped regions, the built-in voltage across the junction is expected to have a magnitude comparable to the material's band-gap. We therefore conclude that the junction built-in voltage is partially screened by the VS shell, and that the measured built-in voltage is only an unscreened fraction.

The study of a p - i - n structure has shown that the intermediate intrinsic segment does not act as a buffer region, but rather as a direct continuation of the p -doped segment, and that both the nominally p - i - n and p - n junction NWs are, in fact, p - n structures, covered by a highly P-doped VS shell. However, while in the former structure, the diode's built-in

voltage is completely screened, it is only partially screened in the latter. A better understanding of the doped VS shell is needed to explain the difference in these results. Towards this end, we simulated a simplified $p-n$ structure, shown schematically in Fig. 4 (a), that consists of two similar silicon segments, one doped with phosphorus and the other with boron, and a phosphorus doped shell on top of them. In the electrostatic model, the silicon core has a radius of 40 nm corresponding to the radius of the VLS grown part of the NW, and each part along the axis is 2 μm , ensuring that the depletion region is contained within the simulated structure and does not reach the simulation boundary (*i.e.* the semiconductor is kept neutral at its edges). The radial doping profile determines the depth of the junction, and therefore directly affects the potential needed to deplete the NW. For both parts of the NW, the radial doping was assumed to have an exponentially decaying profile from the surface toward its center, $N(r) = N(R)\exp[(r-R)/\lambda]$, where $N(r)$ is the doping density at point r , R is the NW radius, $N(R)$ is the doping at the surface (*i.e.* the interface between the VLS core and the VS shell) and λ is the exponential decay coefficient. The doping profile, was chosen following the work of Koren *et al.*,²⁶ and uses similar doping densities at the surface and decay coefficients for both the P and B species. The VS shell thickness t_{vs} was varied between 0.5 and 5 nm, and the doping was varied between 10^{19} and $5 \times 10^{19} \text{cm}^{-3}$. The high P doping of the VS layer results in partial depletion of the B-doped p -type segment. The oxide layer, which may contain fixed charges, was neglected in this simulation since, in contrast to mobile charges and dipoles, fixed charges cannot act as electrostatic screening layers. In prior work, we have shown that the oxide layer is “transparent” in the KPFM when we use an internal reference method as is the case in the present work (the CPD values of the electrode are taken as a reference (zero) value, and are subtracted from the values measured on the NW). The simulation was done using a cylindrical symmetry, which best matches the real device architecture.

While trying to converge the simulation to fit the measured results, it became clear that the built-in voltage observed at the surface is very sensitive to t_{vs} and the VS doping. The graph in Fig. 4 (b) shows observed values of V_{bi} at the surface, as a function of t_{vs} , for two different VS doping levels. At a VS doping of $5 \times 10^{19} \text{cm}^{-3}$, 2 nm of shell is sufficient to reduce the observed V_{bi} from ~ 1 V to ~ 0 V (black curve, Fig. 4 (b)); the actual junction potential is

completely screened. At a VS doping of $2 \times 10^{19} \text{ cm}^{-3}$, (red curve, Fig. 4 (b)) V_{bi} is completely screened at a thickness of 5 nm. Both curves shown in Fig. 4 (b) assume a maximum core doping of $N(R) = 2 \times 10^{19} \text{ cm}^{-3}$. For lower core doping levels (lower $N(R)$), the actual built-in voltage is lower, and the observed V_{bi} on the surface vanishes more quickly with the increase of t_{vs} . We therefore conclude that the doping contrast in the grounded p - i - n NW vanishes completely under the VS shell, whereas the higher contrast in doping levels in the p - n NW results in a residual V_{bi} that is still observable at the surface by KPFM.

Fig. 4 (c) shows a higher resolution KPFM measurement centered at the junction region of the same p - n NW, in reverse bias. The measured profiles (solid lines) are in good agreement with the results of the fitted simulation (dashed lines). We note that despite the small broadening of the measured potential drop around the junction, which is due to a tip-sample convolution effect,³⁰ the measurement is still sufficiently sensitive to changes in the doping levels. In order to find the doping parameters that best fit the measurement, we have first scanned different parameter combinations which yielded the measured V_{bi} of 0.2 V. These combinations were then scanned across the reverse bias range to find the best fit with the measurements. The simulated curves, shown in Fig. 4 (c), correspond to $N(R) = 8 \times 10^{18} \text{ cm}^{-3}$, $\lambda = 20 \text{ nm}$, $t_{\text{vs}} = 3 \text{ nm}$ and VS doping of $2 \times 10^{19} \text{ cm}^{-3}$. These best fitting doping levels, extracted from the simulation, support our previous observation that a high contrast in doping levels is required at the junction for V_{bi} to be, at least partially measurable through the screening VS shell. The high doping levels account also for a narrow depletion width on the surface, as is seen on Fig. 4 (c), which remains smaller than the KPFM spatial resolution ($\sim 30 \text{ nm}$) up to the highest reverse bias measured. The results of the simulation show that the depletion width can be as small as 50 nm at the maximal reverse bias of 2V, on the surface. These small changes of surface depletion length with increasing reverse bias are below the resolution of the KPFM measurement. The simulation shows that the depletion widths increase to up to 110 nm at 10 V, both on the NW's surface and at its core. Fig. 4 (d) shows the electrostatic profile of the NW at reverse bias along the surface (solid lines) and the core, *i.e.* at $r=0$ (dot-dash lines). It is clear that while the potential drop across the junction is larger in the core than on the surface, the depletion width is approximately the same. This relatively large depletion region gives rise to the leakage

currents observed in Fig. 2 (b). Further discussion about the origin of the leakage currents can be found in the Supporting Information. We therefore conclude that the electrostatic junction length is an order of magnitude shorter than the expected doping decay lengths caused by the catalyst reservoir effect. However, the junction is not sufficiently abrupt to induce band-to-band tunneling currents. As a caveat, the simulation does not include the entire circuit, so while the relative magnitudes of leakage and band to band tunneling currents can be compared, their sum is not expected to agree quantitatively with the experimental data. Furthermore, the same approach was not feasible for the *p-i-n* NW due to the absence of a measurable V_{bi} .

4. CONCLUSIONS

We have measured and analyzed the electrostatic properties of VLS *in-situ* doped NW diodes. The two different NW junction profiles give new insights into the effects of simultaneous doping from the liquid catalyst and from the surface. We have shown that the surface potential measured by KPFM is extremely sensitive to the thickness of the VS grown shell and its doping density, and that the junction built-in voltage can become completely screened by the shell. For *p-n* junctions it was shown that an abrupt electric junction on the surface, with low leakage currents can be achieved, despite the diffuse boundaries induced by the catalyst, thanks to the high doping levels. At these high doping levels, the unintentional doping species is quickly compensated by the intentional dopant, thus producing a very narrow transition region between both segments of the diode, in the electrostatic sense. The junction formed in this manner, as seen both in the simulation and the experiment, results in a high quality diode, with leakage currents as low as few nA, and a high current ratio between the on state (taken at +10 V) and the off state (at -1 V) of over five orders of magnitude. We note, however, that this approach requires highly doped junctions, since only high *intentional* doping levels can compensate for the *unintentional* incorporation of dopants from the catalyst reservoir in a rate that will still yield abrupt junctions. These results, along with the suggested model, pave the way for a more informed design of nanostructured devices and components in future electronic applications.

ASSOCIATED CONTENT

Supporting Information: Details of the simulation methodology and a numerical calculation of the contribution of band-to-band tunneling currents to the overall reverse current.

AUTHOR INFORMATION

Notes:

The authors declare no competing financial interests.

ACKNOWLEDGEMENTS

The authors acknowledge the United States-Israel Binational Science Foundation grant 2012088. L.J.L. and N.J. acknowledge the National Science Foundation grant DMR-1308654 for support of this work.

REFERENCES

- (1) Hoffmann, S.; Bauer, J.; Ronning, C.; Stelzner, Th.; Michler, J.; Ballif, C.; Sivakov, V.; Christiansen, S.H. Axial p-n Junctions Realized in Silicon Nanowires by Ion Implantation. *Nano Lett.*, **2009**, *9*, 1341-1344.
- (2) Hazut, O.; Huang, B.-C.; Pantzer, A.; Amit, I.; Rosenwaks, Y.; Kohn, A.; Chang, C.-S.; Chiu, Y.-P.; Yerushalmi, R. Parallel p-n Junctions across Nanowires by One-Step Ex Situ Doping. *ACS Nano*, **2014**, *8*, 8357-8362.
- (3) Christesen, J.D.; Zhang, X.; Pinion, C.W.; Celano, T.A.; Flynn, C.J.; Cahoon, J.F. Design Principles for Photovoltaic Devices Based on Si Nanowires with Axial or Radial p-n Junctions. *Nano Lett.*, **2012**, *12*, 6024-6029.
- (4) Garnett, E.C.; Yang, P. Silicon Nanowire Radial p-n Junction Solar Cells. *J. Am. Chem. Soc.*, **2008**, *130*, 9224-9225.
- (5) Garnett, E.C.; Yang, P. Light Trapping in Silicon Nanowire Solar Cells. *Nano Lett.*, **2010**, *10*, 1082-1087.
- (6) Connell, J.G.; Yoon, K.; Perea, D.E.; Schwalbach, E.J.; Voorhees, P.W.; Lauhon, L.J. Identification of an Intrinsic Source of Doping Inhomogeneity in Vapor-Liquid-Solid-Grown Nanowires. *Nano Lett.*, **2013**, *13*, 199-206.
- (7) Christesen, J.D.; Pinion, C.W.; Zhang, X.; McBride, J.R.; Cahoon, J.F. Encoding Abrupt and Uniform Dopant Profiles in Vapor-Liquid-Solid Nanowires by Suppressing the Reservoir Effect of the Liquid Catalyst. *ACS Nano*, **2014**, *8*, 11790-11798.
- (8) Gamalski, A.D.; Perea, D.E.; Yoo, J.; Li, N.; Olszta, M.J.; Colby, R.; Schreiber, D.K.; Ducati, C.; Picraux, S.T.; Hofmann, S. Catalyst Composition and Impurity-Dependent Kinetics of Nanowire Heteroepitaxy. *ACS Nano*, **2013**, *7*, 7689-7697.
- (9) Perea, D.E.; Hemesath, E.R.; Schwalbach, E.J.; Lensch-Flak, J.L.; Voorhees, P.W.; Lauhon, L.J. Direct Measurement of Dopant Distribution in an Individual Vapour-Liquid-Solid Nanowire. *Nat. Nanotechnol.*, **2009**, *4*, 315-319.
- (10) Amit, I.; Givan, U.; Connell, J.G.; Paul, D.F.; Hammond, J.S.; Lauhon, L.J.; Rosenwaks, Y. Spatially Resolved Correlation of Active and Total Doping Concentrations in VLS Grown Nanowires. *Nano Lett.*, **2013**, *13*, 2598-2604.

- (11) Björk, M.T.; Schmid, H.; Knoch, J.; Riel, H.; Riess, W. Donor Deactivation in Silicon Nanostructures. *Nat. Nanotechnol.*, **2009**, *4*, 103-107.
- (12) Fernández-Serra, M.V.; Adessi, Ch.; Blase, X. Surface Segregation and Backscattering in Doped Silicon Nanowires. *Phys. Rev. Lett.*, **2006**, *96*, 166805.
- (13) Vallett, A.L.; Minassian, S.; Kaszuba, P.; Datta, S.; Redwing, J.M.; Mayer, T.S. Fabrication and Characterization of Axially Doped Silicon Nanowire Tunnel Field-Effect Transistors. *Nano Lett.*, **2010**, *10*, 4813-4818.
- (14) Zavyalov, V.V.; McMurray, J.S.; Williams, C.C. Scanning Capacitance Microscope Methodology for Quantitative Analysis of p-n Junctions. *J. Appl. Phys.*, **1999**, *85*, 7774-7783.
- (15) Peercy, P.S. The Drive to Miniaturization. *Nature*, **2000**, *406*, 1023-1026.
- (16) Jones, E.C.; Ishida, E. Shallow Junction Doping Technologies for ULSI. *Mater. Sci. Eng., R*, **1998**, *24*, 1-80.
- (17) Lu, W.; Lieber, C.M. Semiconductor Nanowires. *J. Phys. D. Appl. Phys.*, **2006**, *39*, R387.
- (18) Léonard, F.; Talin, A.A. Electrical Contacts to One- and Two-Dimensional Nanomaterials. *Nat. Nanotechnol.*, **2011**, *6*, 773-783.
- (19) Mentovich, E.; Belgorodsky, B.; Gozin, M.; Richter, S.; Cohen, H. Doped Biomolecules in Miniaturized Electric Junctions. *J. Am. Chem. Soc.*, **2012**, *134*, 8468-8473.
- (20) He, T.; Corley, D.A.; Lu, M.; Di Spigna, N.H.; He, J.; Nackashi, D.P.; Franzon, P.D.; Tour, J.M. Controllable Molecular Modulation of Conductivity in Silicon-Based Devices. *J. Am. Chem. Soc.*, **2009**, *131*, 10023-10030.
- (21) Schmidt, V.; Wittemann, J.V.; Gösele, U. Growth, Thermodynamics, and Electrical Properties of Silicon Nanowires. *Chem. Rev.*, **2010**, *110*, 361-388.
- (22) Perea, D.E.; Li, Nan.; Dickerson, R.M.; Misra, A.; Picraux, S.T. Controlling Heterojunction Abruptness in VLS-Grown Semiconductor Nanowire via In-situ Catalyst Alloying. *Nano Lett.*, **2011**, *11*, 3117-3122.
- (23) Kallesøe, C.; Mølhave, K.; Larsen, K.F.; Engstrøm, D.; Hansen, T.M.; Bøggild, P.; Mårtensson, T.; Borgström, M.; Samuelson, L. Integration, Gap Formation, and Shapening of III-V Heterostructure Nanowires by Selective Etching. *J. Vac. Sci. Technol. B*, **2010**, *28*, 21.
- (24) Allen, J.E.; Perea, D.E.; Hemesath, E.R.; Lauhon, L.J. Nonuniform Nanowire Doping Profiles Revealed by Quantitative Scanning Photocurrent Microscopy. *Adv. Mater.*, **2009**, *21*, 3067-3072.
- (25) Koren, E.; Berkovitch, N.; Rosenwaks, Y. Measurement of Active Dopant Distribution and Diffusion in Individual Silicon Nanowires. *Nano Lett.*, **2010**, *10*, 1163-1167.
- (26) Koren, E.; Hyun, J.K.; Givan, U.; Hemesath, E.R.; Lauhon, L.J.; Rosenwaks, Y. Obtaining Uniform Dopant Distribution in VLS-Grown Si Nanowires. *Nano Lett.*, **2011**, *11*, 183-187.
- (27) Christesen, J.D.; Pinion, C.W.; Grumstrup, E.M.; Papanikolas, J.M.; Cahoon, J.F. Synthetically Encoding 10 nm Morphology in Silicon Nanowires. *Nano Lett.*, **2013**, *13*, 6281-6286.
- (28) Li, F.; Nellist, P.D.; Cockayne, D.J.H. Doping-Dependent Nanofaceting on Silicon Nanowire Surfaces. *Appl. Phys. Lett.*, **2009**, *94*, 263111.
- (29) Rosenwaks, Y.; Shikler, R.; Glatzel, Th.; Sadewasser, S. Kelvin Probe Force Microscopy of Semiconductor Surface Defects. *Phys. Rev. B.*, **2004**, *70*, 085320.
- (30) Elias, G.; Glatzel, Th.; Meyer, E.; Schwarzman, A.; Boag, A.; Rosenwaks, Y. The Role of the Cantilever in Kelvin Probe Force Microscopy Measurements. *Beilstein J. Nanotechnol.*, **2011**, *2*, 252-260.

Figures

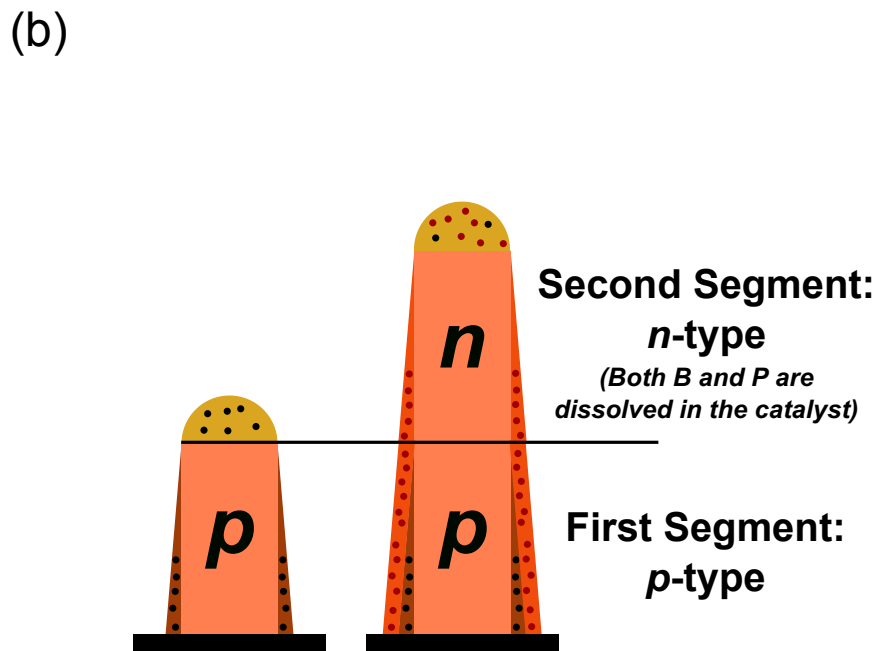
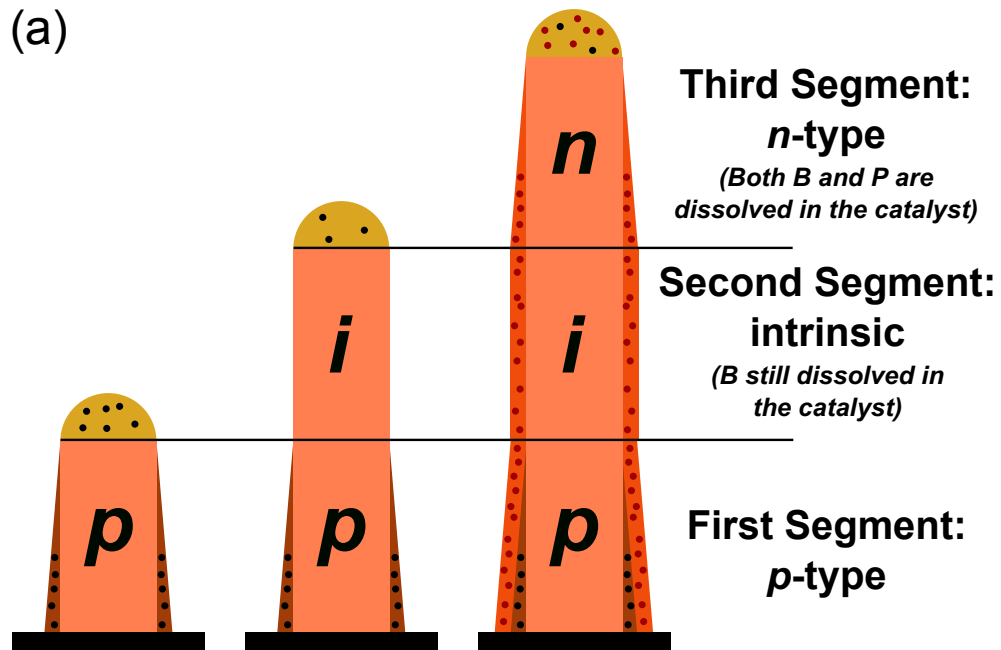


Figure 1: Schematics of the *p-i-n* (a) and *p-n* (b) growth procedure showing the different segments, from left to right. The growth details are given in the text.

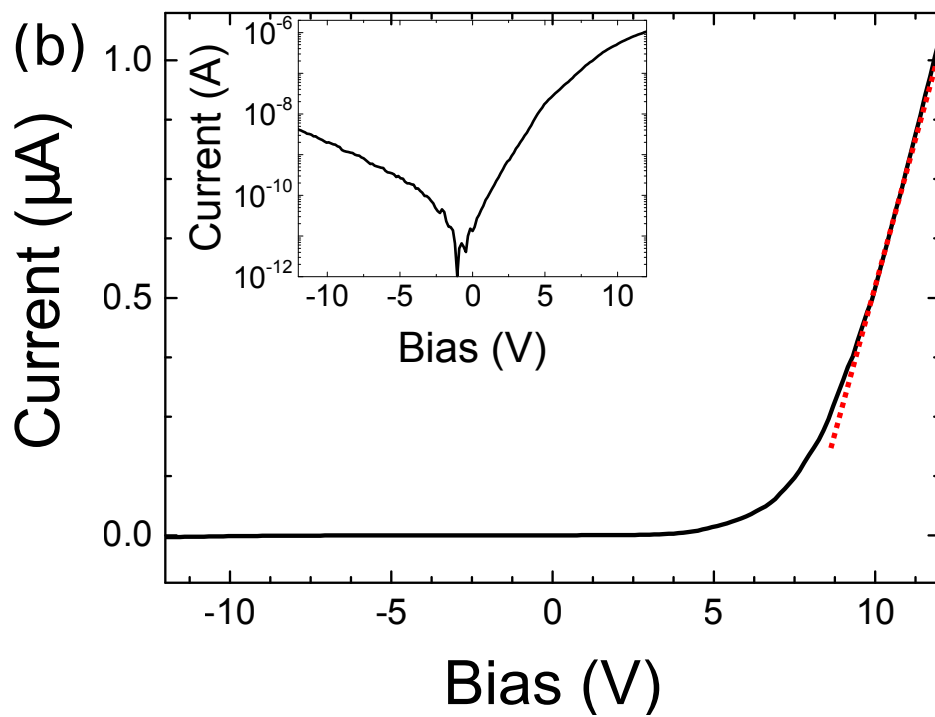
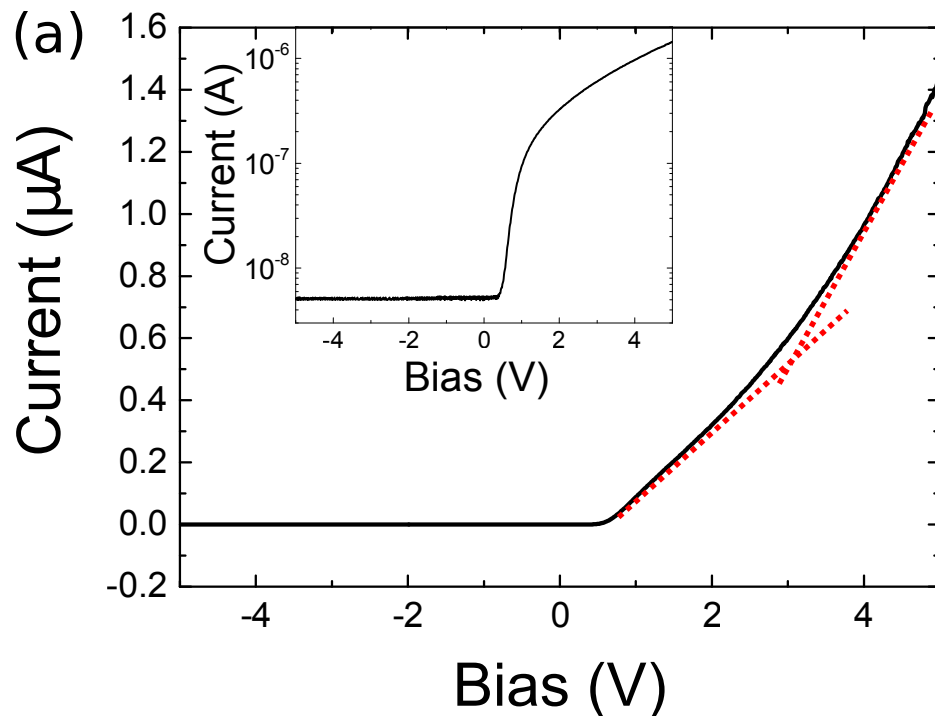


Figure 2: (a+b) Transfer characteristics of a typical $p-i-n$ (a) and $p-n$ (b) NWs. The insets show semi-log plots for the corresponding curves.

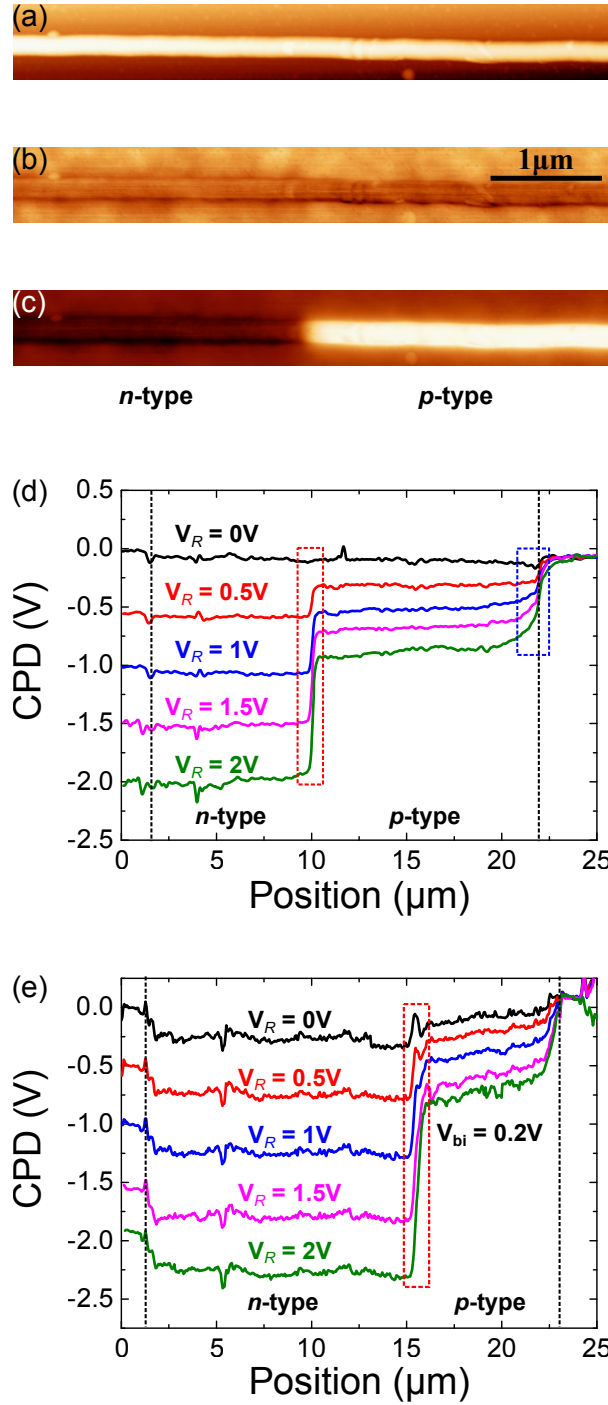


Figure 3: (a+b+c) KPFM images of a p - i - n NW, showing the region around the NW's junction. The three images show the (a) topography (b) CPD when the NW is grounded on both electrodes, and (c) CPD when the wire is reversely biased. (d+e) KPFM scan lines along the (d) p - i - n and (e) p - n wires. V_R stands for reverse bias, the black dashed lines represent the location of the metal electrodes. The dashed red (blue) boxes indicate the location of the p - n (Schottky) junction.

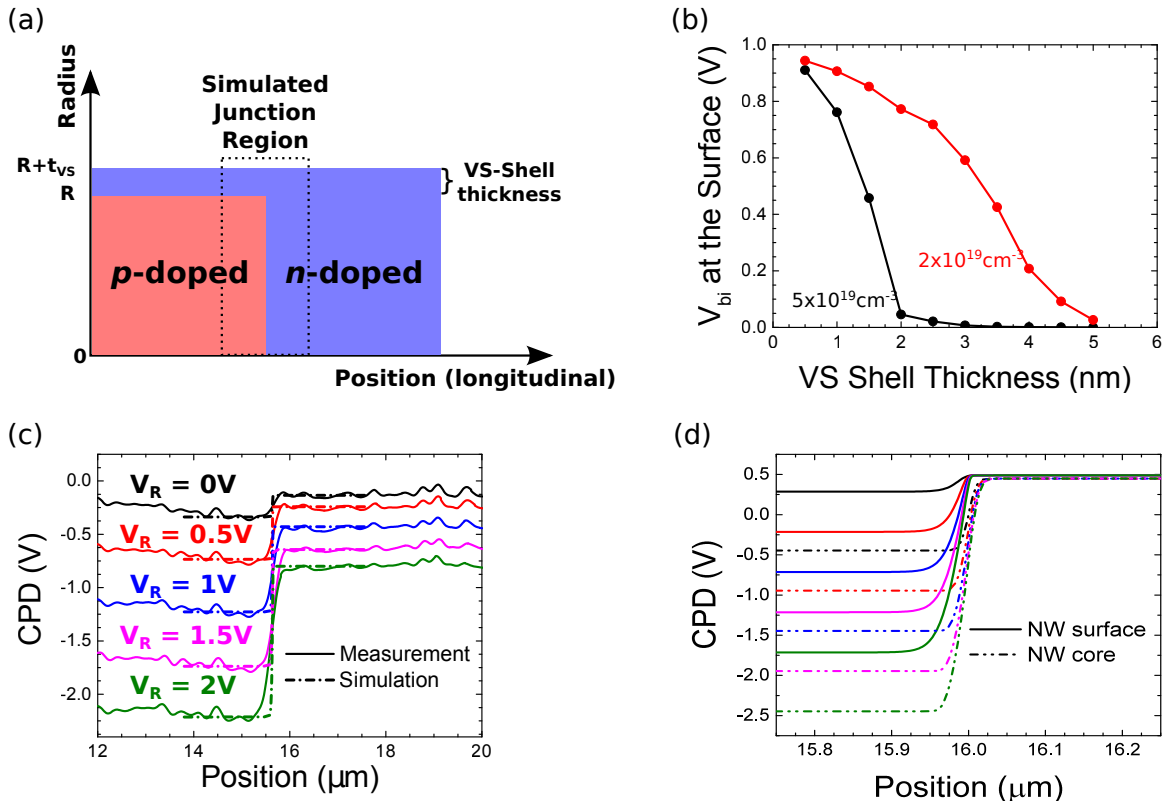


Figure 4: (a) Schematics of the simulation, using the notation described in the text. (b) The simulated V_{bi} on the surface of the wire as a function of the VS shell thickness, for two different VS doping levels. (c) High resolution CPD line profiles of the junction area of a *p-n* NW, in the reverse bias regime, overlaid with the results of the fitted simulation. The extracted parameters are given in the text. (d) A comparison between the simulated electrostatic potential at the surface of the wire (solid lines) and its core (curve-dot lines). The simulation shows that the depletion region is of comparable size along the entire junction depth. The colors represent the same reverse bias values as in panel (c).

TOC graphics

